

Magnetic field dependence of excitations near spin-orbital quantum criticality

A. Biffin,^{1,2} Ch. Rüegg,^{1,3} J. Embs,¹ T. Guidi,⁴ A. Loidl,⁵ V. Tsurkan,^{5,6} and R. Coldea²

¹*Laboratory for Neutron Scattering and Imaging,
Paul Scherrer Institut, 5232 Villigen, Switzerland*

²*Clarendon Laboratory, University of Oxford, Parks Road, Oxford, OX1 3PU, United Kingdom*

³*Department of Quantum Matter Physics, University of Geneva, 1211 Geneva, Switzerland*

⁴*ISIS Facility, Rutherford Appleton Laboratory, Chilton, Didcot, OX11 0QX, United Kingdom*

⁵*Experimental Physics 5, Center for Electronic Correlations and Magnetism,*

Institute of Physics, University of Augsburg, D-86159 Augsburg, Germany and

⁶*Institute of Applied Physics, Academy of Sciences of Moldova, MD-2028, Chisinau, Republic of Moldova*

The spinel FeSc_2S_4 has been proposed to realize a near-critical spin-orbital singlet (SOS) state, where entangled spin and orbital moments fluctuate in a global singlet state on the verge of spin and orbital order. Here we report powder inelastic neutron scattering measurements that observe the full bandwidth of magnetic excitations and we find that spin-orbital triplons of an SOS state can capture well key aspects of the spectrum in both zero and applied magnetic fields up to 8.5 T. The observed shift of low-energy spectral weight to higher energies upon increasing applied field is naturally explained by the entangled spin-orbital character of the magnetic states, a behavior that is in strong contrast to spin-only singlet ground state systems, where the spin gap decreases upon increasing applied field.

When magnetic ions possess an orbital degeneracy in addition to spin, the combined effects of the on-site spin-orbit coupling and the inter-site magnetic exchange interactions have been theoretically proposed to stabilize correlated states with entangled spin-orbital character and novel quasiparticles [1, 2]. Generally such physics is not directly experimentally accessible as symmetry-lowering Jahn-Teller (JT) structural distortions [3] tend to lift orbital degeneracy leaving a spin-only degree of freedom. However, in the case of relatively strong spin-orbit coupling, or certain crystal structures where JT distortions are inhibited by the lattice geometry, spin-orbit entanglement can become manifest. For d^4 [2] and d^6 [4] transition metal ions in certain high-symmetry crystal environments the single-ion ground state is a spin-orbit entangled $J_{\text{eff}} = 0$ singlet with an excited $J_{\text{eff}} = 1$ triplet at higher energy. In this case, a theoretically-proposed phase diagram [1] as a function of the ratio x of magnetic exchange couplings to the singlet-triplet gap λ is shown in Fig. 1 inset. Cooperative spin and orbital order is expected for $x > x_c$, with a novel amplitude (“Higgs”) mode for $x \gtrsim x_c$ [2, 5] and entangled spin-orbital fluctuations present at the critical point x_c . In the regime of moderate exchange interactions, $x \lesssim x_c$, spins and orbitals are expected to be strongly fluctuating in a quantum paramagnetic state denoted as a “spin-orbital singlet” (SOS), with strong correlations between sites [1]. Even though the SOS state has no spin or orbital order, it supports quasiparticles, so called “spin-orbital triplons” (or “spin-orbitons” [6]), corresponding to isotropically-polarized, spin and orbital density wave packets that can propagate coherently across the lattice.

The spinel FeSc_2S_4 has been proposed [1, 7, 8] as a unique candidate to display a SOS state with intermediate-strength exchange interactions ($x \lesssim x_c$)

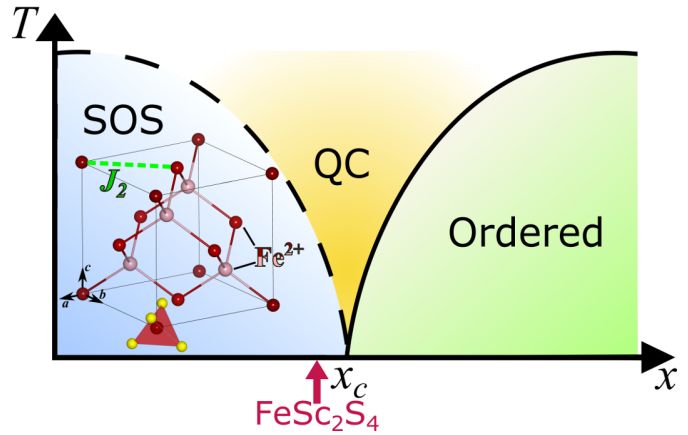


FIG. 1. Proposed phase diagram for systems with spin-orbital singlet state, and structure of FeSc_2S_4 (color online). Generic phase diagram as a function of $x = J_2/\lambda$ [1] with location of FeSc_2S_4 indicated by the vertical arrow. Labels SOS, QC and Ordered stand for spin-orbital singlet, quantum critical, and spin and orbitally ordered, respectively. Solid/dashed line indicates a phase transition boundary/crossover. Inset shows Fe^{2+} ions in FeSc_2S_4 are locally coordinated by a regular tetrahedron (red shaded polyhedron) of S^{2-} atoms (yellow balls) and are arranged in two FCC sublattices (light/dark red balls) with intra-sublattice NN AFM exchange J_2 .

that bring it almost on the verge of spin and orbital order. It is the only known system to explore the physics of highly-dispersive spin-orbital triplons, that may be close to spin-orbital quantum criticality. Here we report inelastic neutron scattering (INS) measurements over the full bandwidth of the magnetic excitations and we find good agreement with the expected spectrum of spin-orbital triplons of a near-critical SOS state. In applied magnetic field we observe a striking shift of the low-energy spectral weight to higher energies upon increasing the magnetic

field, a direct fingerprint of the entangled spin-orbital character of the magnetic states.

FeSc₂S₄ has a cubic crystal structure with space group $Fd\bar{3}m$ (no. 227) and lattice parameter $a = 10.51$ Å at 300 K [9]. Fe²⁺ ions are tetrahedrally-coordinated by S²⁻ and in this crystal field of cubic symmetry the one-electron d orbital states of Fe²⁺ are split into a lower e -doublet and upper t_2 -triplet. Hund's coupling stabilizes a high-spin ($S = 2$) state, $e^3t_2^3$, with a two-fold orbital degeneracy, as the hole can be in either of the two e orbital states. The atomic spin-orbit interaction $\lambda_0 \mathbf{L} \cdot \mathbf{S}$ lifts this two-fold orbital and five-fold spin degeneracy to stabilize a SOS ground state with wavefunction [4]

$$\frac{1}{\sqrt{2}}|3z^2 - r^2\rangle|0\rangle + \frac{1}{2}|x^2 - y^2\rangle(|-2\rangle + |+2\rangle), \quad (1)$$

where for each term the first ket gives the (multi-electron) orbital state and the second ket the S_z eigenvalue. The first excited state is a triplet above a gap λ and local singlet-triplet transitions then form the key ingredient from which coherently-propagating triplons develop in the presence of inter-site exchange interactions.

Previous susceptibility, specific heat and NMR measurements on FeSc₂S₄ [7, 10] showed no clear anomalies indicative of spin or orbital order in spite of strong magnetic interactions manifested by a large antiferromagnetic (AFM) Curie-Weiss temperature of -45 K, indicating that the material may indeed be in the SOS phase. INS studies [8] focusing on the very low energy dynamics indicated that the dominant magnetic interaction is an AFM exchange J_2 between spins located at next-nearest neighbor (NNN) sites. This splits the diamond lattice into two magnetically-decoupled, frustrated FCC lattices (light/dark sites in Fig. 1), where J_2 acts on NN bonds.

We have probed the magnetic excitations using INS measurements first in zero magnetic field and at temperatures 2.2-50 K using the direct-geometry, time-of-flight spectrometer MERLIN at the ISIS neutron source [12]. The sample was a 4 g powder of FeSc₂S₄ synthesized as described in [11] and used in previous thermodynamic and diffraction studies [7]. The INS intensities were converted into absolute units by normalization to data measured on a vanadium standard. For incident neutrons of energy $E_i = 15$ meV the covered phase space observed the full bandwidth of magnetic excitations, which showed prominent dispersions with a bandwidth extending to around 4 meV at the lowest temperatures, as shown in Fig. 2(a). The high-temperature data was used to parameterize and subtract the non-magnetic background (as described in [11]), such that Fig. 2(a) shows the magnetic signal only. Within experimental uncertainty no additional magnetic transitions were detected at higher energy transfers (data collected using incident neutron energies up to 200 meV). This is consistent with the expectation that the single-ion ground state is close to the SOS wavefunction in (1), for which no other (crystal-

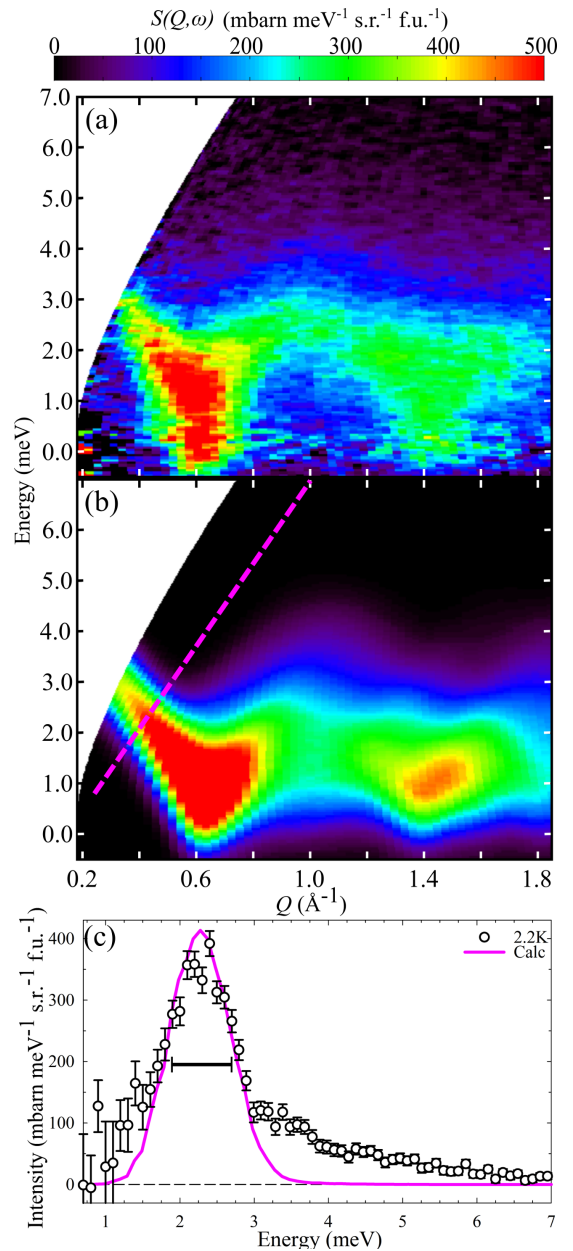


FIG. 2. Spin-orbital triplon excitations in FeSc₂S₄ (color online). (a) Zero field INS data observing highly dispersive magnetic excitations (MERLIN, $E_i = 15$ meV, 12 h counting time, energy resolution 0.79 meV FWHM on the elastic line). Color is intensity with the non-magnetic background subtracted (see [11]). (b) Corresponding one-triplon spectrum including convolution with the instrumental resolution. (c) Intensity along the tilted dashed line direction in (b), compared to the model calculation (solid line). Horizontal bar indicates the expected peak FWHM due to instrumental resolution and spherical averaging. Dashed horizontal line emphasizes that plotted intensities are background subtracted.

field) transitions are symmetry allowed [11]. In agreement with previous low-energy studies [8], we observe a softening of the magnetic excitations near a critical wavevector $Q_S \approx 0.6 \text{ \AA}^{-1}$ [see Fig. 2(a)], whose magnitude coincides with the structurally-forbidden (100) reciprocal lattice position (in units of $2\pi/a$) and a natural wavevector for AFM ordering on the FCC lattice [1]. Higher-resolution measurements shown in Fig. 3(a) indicate a clear suppression of scattering weight below ~ 0.4 meV, indicating that the gap is much smaller than the full bandwidth of the magnetic excitations extending to around 4 meV. This is consistent with the proposal that FeSc_2S_4 is in the very close proximity of the critical point between SOS and magnetic/orbital order, at which the gap would be expected to close [1].

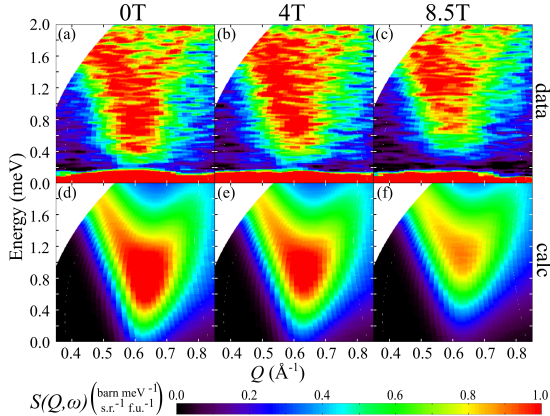


FIG. 3. Low-energy spectrum of FeSc_2S_4 in applied magnetic field (color online). (a-c) Background-subtracted INS data at 0, 4 and 8.5 T magnetic field compared with model calculations (d-f), respectively. The data was collected using FOCUS with $E_i = 3.27$ meV, elastic line energy resolution 0.18 meV FWHM and 11 h counting per setting.

The magnetic field dependence of the excitations was measured on the same powder sample using the FOCUS time-of-flight spectrometer at the Swiss Spallation Neutron Source SINQ (PSI) with the sample placed inside a vertical 9 T cryomagnet. The obtained magnetic INS signal is plotted in Figs. 3(a-c). By comparing the data at different fields it is apparent that the intense V-shaped magnetic signal near Q_S shifts upwards upon increasing field. This trend is directly seen in the energy scan in Fig. 4(a) by comparing the data at 0, 4 and 8.5 T, spectral weight moves to higher energies upon increasing field.

Below we compare quantitatively the dispersive features of the excitation spectrum and the observed magnetic field dependence of the low-energy scattering with a model of spin-orbital triplons of a SOS ground state. In zero field the triplon dispersion derived in the harmonic approximation using pseudo-boson operators [11]

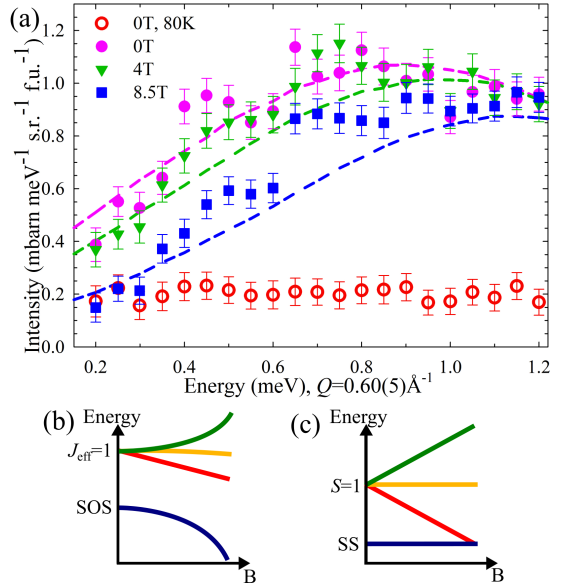


FIG. 4. Behaviour of the gap in magnetic field (color online). (a) Energy scan at the softening wavevector Q_S through the background-subtracted data in Fig. 3(a-c): filled circles, triangles and squares denote fields of 0, 4 and 8.5 T, respectively. Dashed lines of the same color are the model calculation shown in Fig. 3(d-f). The same data at 0 T in the paramagnetic phase at high temperatures (80 K) is also included (red open circles). b) Schematic (not to scale) diagram of the ground and excited states energies as a function of applied field in the case of a SOS system, and a spin-singlet system (c).

or alternative methods [13] is

$$\hbar\omega(\mathbf{k}) = \lambda \sqrt{1 + \frac{4J(\mathbf{k})}{\lambda}}, \quad (2)$$

where $J(\mathbf{k}) = J_2 \sum_{\mathbf{A}} \cos(\mathbf{k} \cdot \mathbf{A})$ is the Fourier transform of the exchange couplings and \mathbf{A} runs over all NN vectors of an FCC sublattice. The local singlet-triplet gap λ is determined by the crystal field strength (parameterized using standard convention [14] by the single parameter $B_4 < 0$, and the atomic spin-orbit coupling $\lambda_0 < 0$). Within a minimal (J_2, B_4, λ_0) model we calculate the powder-averaged INS spectrum including the triplons' dynamical structure factor (for details see [11]) and compare systematically with scans through the INS data as shown in Figs. 2(c) and 4(a) (magenta filled symbols). In addition, we require the model parameters to reproduce optical data: the sharp 4.46 meV absorption in THz spectroscopy [6, 15], identified with the triplon energy (2) at the zone center, $\hbar\omega(\mathbf{0}) = \sqrt{\lambda(\lambda + 48J_2)}$, and the sharp optical absorption at $\hbar\Omega = 262(2)$ meV, attributed to the transition from the ground state to the lowest level of the upper orbital triplet [16]. Using those multiple constraints the best fit parametrization is obtained for $J_2 = 0.136(6)$ meV, $B_4 = -2.45(6)$ meV and

$\lambda_0 = -12.1(1)$ meV, which give $\lambda = 2.28(6)$ meV [17]. This parametrization reproduces (by construction) the energies of both optical transitions and the J_2 value is comparable to that deduced from Curie-Weiss fits of the high-temperature susceptibility [15] and estimated from density-functional calculations [18]. The B_4 and λ_0 values are comparable with -2.58 and $-10.0(9)$ meV, respectively, found for Fe^{2+} ions in FeCr_2S_4 [19].

The INS spectrum for the fitted parameter values is shown in Fig. 2(b), where we have also included an intrinsic linewidth broadening ~ 1 meV, a possible significance of this broadening will be discussed later. The parametrization by the minimal model captures well the key features of the INS data with clear V-shaped dispersions and mode softenings near 0.6 and 1.4 \AA^{-1} , identified with scattering emanating near the reciprocal lattice positions (100) and (211) , respectively. A corresponding calculation performed for the data measured on FOCUS at zero field is shown in Fig. 3(d) and this also compares well with the data in panel (a). Energy scans near the softening wavevector are in good agreement between the data and model [see Fig. 4(a), magenta filled symbols/line]. Fig. 2(c) shows also the limitations of the present model. The energy scan shown cuts across the low- Q dispersion and the model (solid line) reproduces well the observed peak position. However, the linewidth is broader than expected based on resolution effects alone (horizontal bar) and there is considerable additional continuum scattering intensity at higher energies above 3 meV, which we attribute to multi-triplon scattering events, not included in the present model.

With the model parameters kept fixed by the fits to zero-field data, we now calculate the expected behavior in an external magnetic field, which contributes additional terms to the single-ion Hamiltonian; $\mu_B \mathbf{B} \cdot (\mathbf{L} + 2\mathbf{S}) + 12J_2 \mathbf{S} \cdot \langle \mathbf{S} \rangle$. The first term is the Zeeman energy in field and the second term includes the effect of the exchange interactions, treated in a mean-field approximation [20]. $\langle \mathbf{S} \rangle$ is the field-induced spin polarization of the ground state, i.e. $\langle \mathbf{S} \rangle = \langle \psi_0 | \mathbf{S} | \psi_0 \rangle$, where ψ_0 is the ground state wavefunction of the single-site Hamiltonian. Solving for $\langle \mathbf{S} \rangle$ self-consistently we find the wavefunctions $\psi_{1,2,3}$ and energies $\lambda_{1,2,3}$ for a general field direction, determine the triplon dispersion relations and neutron structure factor, then average the spectrum over a spherically uniform distribution of powder grains (see [11] for details). The model calculations are compared with the measured INS data in Fig. 3, panels (e-f) with (b-c) at 4 and 8.5 T; the model captures the apparent upwards shift of the scattering intensity upon increasing field. This is even more clearly seen in the energy scans in Fig. 4(a), the model calculation (dashed lines) reproduce well the observed shift of spectral weight to higher energies upon increasing field with no adjustable parameters once the overall intensity scale factor is fixed by the comparison in zero field.

It is insightful to compare the spin-orbital triplons of a SOS ground state discussed here with triplons of a spin-singlet (SS) ground state with completely quenched orbital degree of freedom, as found for example in quantum dimerized antiferromagnets like TlCuCl_3 [21]. For the latter, a magnetic field Zeeman splits the triplet into $S_z = -1, 0, +1$ states, with a linear reduction in the gap to the $S_z = -1$ state, as shown schematically in Fig. 4(c). At a critical field level crossing with the ground state occurs and magnetic order ensues via condensation of triplons. One might wonder how the behavior of spin-orbital triplons can be any different; the triplons now have an effective angular momentum $J_{\text{eff}} = 1$ (as opposed to $S = 1$ in the SS case). A low applied magnetic field Zeeman splits the triplet into $J_{\text{eff},z} = -1, 0, +1$ states [4, 15], however at higher fields terms quadratic and higher in B prevail [13, 22] and allow mixing between the SOS and the $J_{\text{eff},z} = 0$ triplet mode. This enables the ground state to *reduce* its energy in applied field by acquiring a finite polarization along the field direction, see Fig. 4(b), thus avoiding magnetic order via level crossing with the triplet states. Instead the SOS state is further stabilized by an applied magnetic field.

We now relate our results to the generic phase diagram in Fig. 1, describing the transition from SOS to magnetic/orbital order upon increasing $x = J_2/\lambda$. Using the parameters obtained from fitting the INS data yields $x \simeq 0.060$, marginally close to the proposed critical value $x_c = 1/16$. For such close proximity to criticality one might expect manifestations of enhanced quantum fluctuations associated with the critical point. For $x \lesssim x_c$ in addition to sharp triplon excitations one would also expect multi-triplon continua at higher energies, with enhanced spectral weight and decreasing gap as $x \nearrow x_c$, with the triplon dispersions becoming lower boundaries of a critical continuum of excitations precisely at the quantum critical point at x_c . Effects associated with such continuum scattering and/or broadening of sharp modes may be at least partly responsible for the extra scattering intensity and broadening effects observed in the INS data in Fig. 2(c), we hope our results will stimulate further theoretical modelling of such effects close to spin-orbital quantum criticality.

One may ask if other materials may exhibit related physics. We note that a high-spin d^4 ion (e.g. Mn^{3+}) in an octahedral (weak) cubic crystal field displays the same single-ion physics (*electron* analogue) as Fe^{2+} in FeSc_2S_4 , i.e. spin $S = 2$ and *two*-fold orbital degeneracy, where the spin-orbit coupling (now $\lambda_0 > 0$) stabilizes the SOS ground state in (1) with a $J_{\text{eff}} = 1$ excited triplet. Similar singlet-triplet physics, but with a singlet ground state distinct from (1), originating from $S = 1$ and *three*-fold orbital degeneracy, is expected for low-spin d^4 ions (e.g. Ru^{4+}) in strong octahedral crystal field [2, 5] and d^8 ions (e.g. Ni^{2+}) in tetrahedral field. We have explicitly verified by direct calculation of the wavefunctions that at

the single-ion level *all* the above cases have qualitatively the same behavior in applied field, i.e. the singlet state is stabilized as shown in Fig. 4(b). If such ions can resist JT distortions, they are candidates to display correlated spin-orbit states under inter-site exchange, potentially in a different part of the phase diagram in Fig. 1, where applied fields could be used to stabilize the quantum paramagnetic phase.

To summarize, we have reported powder INS measurements of the full bandwidth of magnetic excitations in the spinel FeSc_2S_4 and have found that the key dispersive features can be well described by spin-orbital triplons of a near-critical SOS state. In high applied magnetic field we have observed a shift of spectral weight to higher energies, giving support to the theoretical proposal [20] that applied fields further stabilize the SOS state by moving the system away from the quantum critical point, this is a direct consequence of the entangled spin-orbital nature of the ground and excited triplet states.

This work was partially supported by the EPSRC (U.K) under Grant No. EP/H014934/1, as well as the SNF SCOPES project IZ73Z0_152734/1, the Marie Curie FP7 COFUND PSI Fellowship program, Swiss National Science Foundation, Sinergia Network Mott Physics Beyond the Heisenberg Model and Transregional Research Collaboration TRR 80 (Augsburg, Munich, Stuttgart). This work is partially based on experiments performed at the Swiss spallation neutron source SINQ, Paul Scherrer Institute, Villigen, Switzerland.

Note added. As this work was being completed Ref. [23] appeared, reporting evidence for marginal magnetic order in samples synthesized using a different protocol, suggesting an extreme sensitivity to the synthesis route. Our results highlighting that magnetic fields favor the SOS state suggest a very interesting possibility that fields applied onto an ordered sample, potentially along a particular direction in a single crystal, may drive it towards the SOS state and thus reach the long-searched-for quantum critical point.

[1] G. Chen, L. Balents, and A. P. Schnyder, Phys. Rev. Lett. **102**, 096406 (2009).

[2] G. Khaliullin, Phys. Rev. Lett. **111**, 197201 (2013).

[3] H. A. Jahn and E. Teller, Proc. Roy. Soc A: Math. Phys. Eng. Sci. **161**, 220 (1937).

[4] W. Low and M. Weger, Phys. Rev. **118**, 1119 (1960).

[5] A. Jain, J. Krautloher, M. Porras, G. H. Ryu, D. P. Chen, D. L. Abernathy, J. T. Park, A. Ivanov, J. Chaloupka, G. Khaliullin, B. Keimer, and B. J. Kim, arXiv:1510.07011 .

[6] L. Mittelstädt, M. Schmidt, Z. Wang, F. Mayr, V. Tsurkan, P. Lunkenheimer, D. Ish, L. Balents, J. Deisenhofer, and A. Loidl, Phys. Rev. B **91**, 125112 (2015).

[7] V. Fritsch, J. Hemberger, N. Büttgen, E.-W. Scheidt, H. Krug von Nidda, A. Loidl, and V. Tsurkan, Phys. Rev. Lett. **92**, 116401 (2004).

[8] A. Krimmel, M. Mücksch, V. Tsurkan, M. Koza, H. Mutka, and A. Loidl, Phys. Rev. Lett. **94**, 237402 (2005).

[9] P. A. Tomas and M. Guittard, Matt. Res. Bull. **14**, 249 (1979).

[10] N. Büttgen, a. Zymara, C. Kegler, V. Tsurkan, and A. Loidl, Physical Review B **73**, 132409 (2006).

[11] A. Biffin, C. Rüegg, J. Embs, T. Guidi, V. Tsurkan, and R. Coldea, Supplemental information.

[12] R. Bewley, R. Eccleston, K. McEwen, S. Hayden, M. Dove, S. Bennington, J. Treadgold, and R. Coleman, Physica B: Condensed Matter **385-386**, 1029 (2006).

[13] D. Ish and L. Balents, Phys. Rev. B **92**, 094413 (2015).

[14] A. Abragam and B. Bleaney, *Electron Paramagnetic Resonance of Transition Ions*, “1st” ed. (Dover, 1970).

[15] N. J. Laurita, J. Deisenhofer, L. Pan, C. M. Morris, M. Schmidt, M. Johnsson, V. Tsurkan, A. Loidl, and N. P. Armitage, Phys. Rev. Lett. **114**, 207201 (2015).

[16] As discussed in [15, 24], the transition from the ground state to the lowest level of the orbital triplet occurs at $\hbar\Omega = \hbar\Omega_0 - E_{JT}$, where E_{JT} is an energy shift due to the coupling to Jahn-Teller phonons. We have used the estimate $E_{JT} \approx 7$ meV [15] to deduce the energy of the purely electronic transition $\hbar\Omega_0$ and this was then used in the data parameterization to constrain B_4 and λ_0 .

[17] Note that the usually-assumed lowest order approximation $\lambda \approx 6\lambda_0^2/(120|B_4|)$ [4] would predict a value $\sim 30\%$ higher than that obtained from directly calculating the energy levels of the full single-ion Hamiltonian.

[18] S. Sarkar, T. Maitra, R. Valentí, and T. Saha-Dasgupta, Phys. Rev. B **82**, 041105 (2010).

[19] L. F. Feiner, Journal of Physics C: Solid State Physics **15**, 1515 (1982).

[20] G. Chen, A. P. Schnyder, and L. Balents, Phys. Rev. B **80**, 224409 (2009).

[21] C. Rüegg, B. Normand, M. Matsumoto, A. Furrer, D. McMorrow, K. Krämer, H. Güdel, S. Gvasaliya, H. Mutka, and M. Boehm, Phys. Rev. Lett. **100**, 205701 (2008).

[22] The *g*-factor characterizing the linear splitting is predicted [13] to be wavevector-dependent and vary as the square of the zero-field triplon energy in (2), therefore to become negligibly small near the magnetic softening wavevector, where the regime of linear splitting of the triplet modes is practically unobservable as quadratic and higher order terms in *B* dominate.

[23] K. W. Plumb, J. Morey, J. A. Rodriguez-Rivera, H. Wu, A. A. Podlesnyak, T. M. McQueen, and C. L. Broholm, (2016), arXiv:1603.08033.

[24] S. Wittekoek, R. P. van Stapele, and A. W. J. Wijma, Phys. Rev. B **7**, 1667 (1973).

[25] M. Hutchings, *Point-Charge Calculations of Energy Levels of Magnetic Ions in Crystalline Electric Fields*, “1st” ed. (OUP, 1963).

[26] C. Testelin, C. Rigaux, A. Mauger, A. Mycielski, and C. Julien, Phys. Rev. B **46**, 2183 (1992).

[27] B. Grover, Phys. Rev. **140**, 1944 (1965).

[28] R. M. White, M. Sparks, and I. Ortenburger, Phys. Rev. **139**, 450 (1965).

[29] A. G. D. Maestro and M. J. P. Gingras, J. Phys. Cond. Matt. **16**, 3339 (2004).

[30] G. Squires, *Introduction to the Theory of Thermal Neu-*

tron Scattering, “1st” ed. (Cambridge University Press, 1978).

SUPPLEMENTAL MATERIAL

Here we outline 1) the derivation of the spin-orbital wavefunctions for a single Fe^{2+} ion in a tetrahedral cubic crystal field including spin-orbit coupling, 2) the description of the lowest singlet-triplet transition in terms of spin-orbital triplon operators, 3) the analytic derivation of the triplon dispersions in the presence of magnetic exchange interactions and the relevant matrix elements for neutron scattering, 4) the derivation of single-ion states in the presence of an external magnetic field and exchange via a mean-field approach, 5) the non-magnetic background subtraction procedure for the INS data via the principle of detailed balance, 6) the derivation of the neutron cross-section for triplon scattering and spherical averaging to compare with powder INS data, and 7) details on the sample preparation for the FeSc_2S_4 powder used in the INS experiments.

S1. SINGLE ION HAMILTONIAN

This section outlines the derivation of the spin-orbital wavefunctions for a single Fe^{2+} ($3d^6$) ion in the (weak) crystal field environment appropriate for FeSc_2S_4 . The Hamiltonian is

$$\mathcal{H} = \mathcal{H}_{\text{cf}} + \mathcal{H}_{\text{SO}} + \mathcal{H}_{\text{Zeeman}}, \quad (\text{S1})$$

where the three terms are the crystal field, spin-orbit and external magnetic field contributions, respectively. The crystal-field term can be expressed via the equivalent operator method in terms of Stevens operators of the orbital angular momentum \mathbf{L} . The allowed terms are constrained by the local site symmetry and for a cubic environment \mathcal{H}_{cf} is of the form [14]

$$\mathcal{H}_{\text{cf}} = B_4(O_4^0 + 5O_4^4),$$

where O_4^0 and O_4^4 are Stevens operators (tabulated in [25]) and B_4 is a constant that characterizes the strength of the crystal field ($B_4 < 0$ for a d^6 ion in tetrahedral coordination). In expanded form the crystal-field Hamiltonian reads

$$\mathcal{H}_{\text{cf}} = B_4([35L_z^4 - 30L(L+1)L_z^2 + 25L_z^2 - 6L(L+1) + 3L^2(L+1)^2] + \frac{5}{2}[L_+^4 + L_-^4]), \quad (\text{S2})$$

where the Cartesian x, y, z axes are chosen along the cubic axes of the unit cell.

The second term in (S1) is the atomic spin-orbit interaction,

$$\mathcal{H}_{\text{SO}} = \lambda_0 \mathbf{L} \cdot \mathbf{S}, \quad (\text{S3})$$

with $\lambda_0 < 0$ for a d^6 ion (hole-like). For calculation purposes it is helpful to expand the dot product as

$$\mathbf{L} \cdot \mathbf{S} = L_z S_z + \frac{1}{2} (L_+ S_- + L_- S_+),$$

where the \pm ladder operators are the standard ones, i.e. $L_{\pm}|L, M_L\rangle = \sqrt{(L \mp M_L)(L \pm M_L + 1)}|L, M_L \pm 1\rangle$ and similar for S_{\pm} .

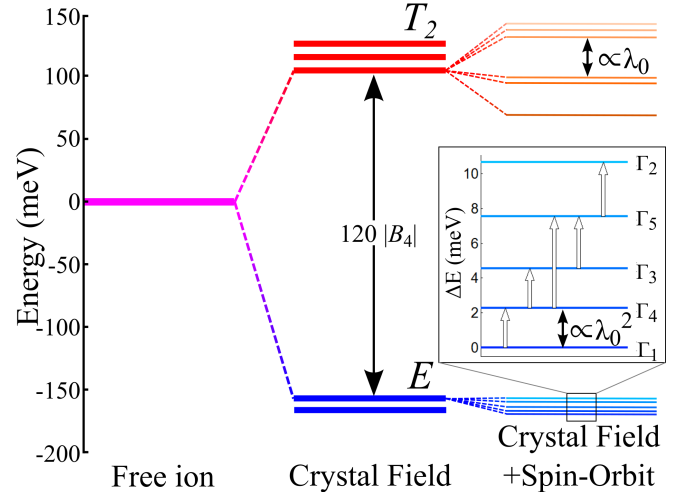


FIG. S1. (Color online) Splitting of Fe^{2+} free ion orbital levels due to crystal field and spin-orbit coupling. Inset: Allowed transitions via neutron scattering for the 5 states derived from the E -doublet where side labels Γ_1 – Γ_5 indicate the corresponding irreducible representations (from [26]).

The Fe^{2+} ($3d^6$) ions are in an $S = 2, L = 2$ configuration. We use the $|M_L, M_S\rangle$ states as basis to describe the wavefunctions, where M_L and M_S are the projections of the \mathbf{L} and \mathbf{S} operators onto the quantization axis z , each takes values of $-2 \dots 2$. In this basis all operators are represented by 25×25 matrices and diagonalization of the Hamiltonian (S1) obtains the spectrum of states shown in Fig. S1. The cubic crystal field splits the 5-fold degenerate $L = 2$ orbital states into a lower E -doublet and upper T_2 -triplet above a gap $\Delta_{\text{cf}} = -120B_4 > 0$ (same level splitting, symmetry of wavefunctions and order of levels as for a single d -electron with orbital quantum number $l = 2$). The spin-orbit coupling further splits those levels. At lowest order in λ_0 , the upper T_2 manifold is split into three levels with energies $\Delta_{\text{cf}} - 3\lambda_0$, $\Delta_{\text{cf}} - \lambda_0$ and $\Delta_{\text{cf}} + 2\lambda_0$, and the E manifold is split into 5 equidistant levels separated by $6\lambda_0^2/\Delta_{\text{cf}}$ [4]. The last column in Fig. S1 indicates those lowest five levels and their irreducible representations, the ground state is a singlet and the first excited state a triplet. Transitions between states probed via neutron scattering are determined by the matrix element

$$\langle f | \mathbf{L} + 2\mathbf{S} | i \rangle, \quad (\text{S4})$$

where $|i\rangle$ and $|f\rangle$ denote the initial and final states, respectively. The symmetry-allowed transitions between levels originating from the lower E -doublet are indicated by thick white arrows in Fig. S1 last column.

Note that the three degenerate states of the first excited triplet can be described by an effective angular momentum $J_{\text{eff}} = 1$ with $\psi_{1,2,3}$ identified as eigenstates of $J_{\text{eff},z}$ with eigenvalues of $-1, 0, +1$ respectively. To obtain the explicit wavefunctions of those states (listed in Table S1) we solve for the eigenstates in the presence of an infinitesimally small applied magnetic field $\mathbf{B} \parallel (001)$ (to be discussed later) and then choose appropriate relative signs in front of the obtained wavefunctions such that they satisfy the operator algebra for the total angular momentum $\mathbf{J} = \mathbf{L} + \mathbf{S} \equiv \alpha \mathbf{J}_{\text{eff}}$. Explicitly, the matrix representations of the operators J_z and J_+ in the basis of $\psi_{1,2,3}$ states are found to be

$$J_z = \alpha \begin{pmatrix} -1 & 0 & 0 \\ 0 & 0 & 0 \\ 0 & 0 & 1 \end{pmatrix}, \quad J_+ = \alpha \begin{pmatrix} 0 & 0 & 0 \\ \sqrt{2} & 0 & 0 \\ 0 & \sqrt{2} & 0 \end{pmatrix}$$

where the projection factor is $\alpha \approx 0.44$ for the B_4 and λ_0 values used in the analysis ($\alpha \rightarrow 1/2$ as $|B_4| \rightarrow \infty$).

We have explicitly verified that the wavefunctions obtained agree with previous studies [14, 26] of Fe^{2+} ions in cubic crystal-field environments. Furthermore, we have verified that the spin-orbit coupling only mixes states belonging to the same irreducible representation, as expected from symmetry considerations. For example, the ground state wavefunction in Table S1 can be written as

$$\begin{aligned} \psi_0 \approx & 0.984 \times \left[\frac{1}{\sqrt{2}} |3z^2 - r^2\rangle |S^z = 0\rangle \right. \\ & + \frac{1}{2} |x^2 - y^2\rangle (|S_z = -2\rangle + |S_z = 2\rangle) \left. \right] \\ & - 0.178 \times \frac{1}{\sqrt{3}} \left[\frac{1}{\sqrt{2}i} |xy\rangle (|S_z = 2\rangle - |S_z = -2\rangle) \right. \\ & + \frac{1}{\sqrt{2}i} |yz\rangle (-|S_z = 1\rangle - |S_z = -1\rangle) \\ & \left. + \frac{1}{\sqrt{2}} |zx\rangle (|S_z = -2\rangle + |S_z = 2\rangle) \right], \end{aligned} \quad (\text{S5})$$

where the usual notation for d -orbitals has been used. In the above expansion the first term is the “ideal” SOS state in (1) (obtained in the limit $|B_4| \rightarrow \infty$). The second term in (S5) is a singlet state originating from the T_2 level, mixed in by the spin-orbit coupling.

In a finite magnetic field the single-ion Hamiltonian (S1) acquires a Zeeman term,

$$\mathcal{H}_{\text{Zeeman}} = \mu_B \mathbf{B} \cdot (\mathbf{L} + g_S \mathbf{S}), \quad (\text{S6})$$

where we assume $g_S = 2$ for spin. The magnetic field dependence of the energy levels of the four lowest states is schematically illustrated in Fig. 4(b), the three lowest excited states $\psi_{1,2,3}$ have now distinct energy gaps $\lambda_{1,2,3}$ above the ground state. In the limit of small applied field the behavior is isotropic, independent of the applied field direction, and the splitting of the triplet states can

$ M_L, M_S\rangle$	ψ_0	ψ_1	ψ_2	ψ_3
$ 2, 2\rangle$	0.399	-	-0.571	-
$ 2, 1\rangle$	-	-0.371	-	-
$ 2, -1\rangle$	-	-	-	0.326
$ 2, -2\rangle$	0.297	-	0.416	-
$ 1, 2\rangle$	-	-0.032	-	-
$ 1, 0\rangle$	-	-	-	0.135
$ 1, -1\rangle$	0.102	-	0.032	-
$ 1, -2\rangle$	-	-0.078	-	-
$ 0, 1\rangle$	-	-	-	0.855
$ 0, 0\rangle$	0.696	-	-	-
$ 0, -1\rangle$	-	-0.855	-	-
$ -1, 2\rangle$	-	-	-	0.078
$ -1, 1\rangle$	0.102	-	-0.032	-
$ -1, 0\rangle$	-	-0.135	-	-
$ -1, -2\rangle$	-	-	-	0.032
$ -2, 2\rangle$	0.297	-	-0.416	-
$ -2, 1\rangle$	-	-0.326	-	-
$ -2, -1\rangle$	-	-	-	0.372
$ -2, -2\rangle$	0.399	-	0.572	-

TABLE S1. The wavefunctions ψ_{0-3} of the four lowest energy single-ion states for $\lambda_0 = -12.1$ meV and $B_4 = -2.45$ meV ($B=0$) expressed in the 25-element basis of $|M_L, M_S\rangle$ states. For those parameters the energy gap for the transition $\psi_0 \rightarrow \psi_{1,2,3}$ is $\lambda = 2.28$ meV. Note that the lowest order approximation $\lambda \approx 6\lambda_0^2/(120|B_4|)$ is not applicable for the present case as it would predict a $\sim 30\%$ higher value than obtained from directly calculating the energy levels of the full single-ion Hamiltonian in (S1).

be described by an effective Zeeman term $\mathcal{H}_{\text{Zeeman, eff}} = g\mu_B \mathbf{B} \cdot \mathbf{J}_{\text{eff}}$. For the B_4 and λ_0 values used here the g -factor is obtained as $g \approx 0.94$. For moderate magnitude applied fields (when the Zeeman energy is comparable to the zero-field gap λ) the splitting of the excited triplet is non-linear, cannot be described in terms of the simplified $J_{\text{eff}} = 1$ states, and furthermore is strongly dependent on the applied field direction with respect to the cubic axes, so in the general case we determine the wavefunctions ψ_{0-4} of the four lowest states and the gaps λ_{1-3} via a direct diagonalization of the full single-ion Hamiltonian in (S1).

S2. PSEUDO-BOSON OPERATORS

In this section we introduce pseudo-boson operators to describe the transitions from the ψ_0 ground state singlet to the $\psi_{1,2,3}$ excited triplet states to have a physical basis to describe the magnetic dynamics. At very low temperatures only the ψ_0 ground state is thermally populated and the only symmetry-allowed transitions in

neutron scattering are to the $\psi_{1,2,3}$ states. So to capture the magnetic dynamics observable by neutron scattering it is sufficient to consider the restricted set of those four basis states and construct matrix representations of all operators in this restricted basis, i.e. for a general operator \hat{O} this would be

$$\hat{O} = \begin{bmatrix} \langle \psi_0 | \hat{O} | \psi_0 \rangle & \langle \psi_0 | \hat{O} | \psi_1 \rangle & \dots \\ \langle \psi_1 | \hat{O} | \psi_0 \rangle & \langle \psi_1 | \hat{O} | \psi_1 \rangle & \dots \\ \vdots & \vdots & \ddots \end{bmatrix}. \quad (\text{S7})$$

An alternative description of the restricted set of basis states is in terms of occupation numbers of three types of pseudo-bosons [27], where the ground state ψ_0 is interpreted as the ‘vacuum’, the excited ψ_1 state corresponds to having one a -type boson present, the ψ_2 has one b -type boson, and so on. Explicitly, the creation operators for the three types of bosons are defined as

$$\begin{aligned} a^\dagger \psi_0 &= \psi_1, \\ b^\dagger \psi_0 &= \psi_2, \\ c^\dagger \psi_0 &= \psi_3, \end{aligned} \quad (\text{S8})$$

where the annihilation operators are obtained by Hermitian conjugation as $a\psi_1 = \psi_0$ and so on. The pseudo-boson operators have a trivial matrix representation in terms of the four-basis states ψ_{0-3} , i.e. the creation operator for a -type bosons is represented as

$$a^\dagger = \begin{bmatrix} 0 & 0 & 0 & 0 \\ 1 & 0 & 0 & 0 \\ 0 & 0 & 0 & 0 \\ 0 & 0 & 0 & 0 \end{bmatrix}. \quad (\text{S9})$$

By comparing (S7) and representations of the type shown in (S9) it is clear that the 4×4 matrix representation of a general operator may be equivalently expressed as a sum of linear and bilinear terms in the boson creation/annihilation operators, and the identity operator. Therefore, once the wavefunctions ψ_{0-3} are known explicitly, then the 4×4 matrix representation of all relevant spin and orbital operator components such as S_z, L_z, \dots can be constructed, and those can then be expanded in terms of boson operators.

33. DISPERSION OF TRIPLONS

In this section we outline the derivation of the dispersion relations of magnetic excitations in the harmonic approximation using the pseudo-boson operators defined in the previous section. In the presence of magnetic exchange interactions between Fe^{2+} sites the local singlet-triplet transitions acquire a dispersion, i.e. the pseudo-bosons become delocalized by hopping across lattice sites. This leads to coherently-propagating excitations, so-called ‘spin-orbital triplons’ due to the mixed

spin-orbital character and the three-fold degeneracy (in zero field).

We assume in a first approximation that the global ground state is the same as in the non-interacting case, given by the product of the $\psi_0(\mathbf{r})$ single-ion states at all sites \mathbf{r} in the lattice, and we focus on the effects of the exchange interactions on the singlet-triplet transition. Considering a minimal model with a Heisenberg antiferromagnetic exchange interaction $J_2 > 0$, the Hamiltonian for each of the two magnetically-decoupled FCC sublattices reads

$$\mathcal{H}_{\text{ex}} = \sum_{\langle ij \rangle} J_2 \mathbf{S}_i \cdot \mathbf{S}_j, \quad (\text{S10})$$

where the sum extends over all ij NN pairs of sites, with each pair counted once. In expanded form this reads

$$\mathcal{H}_{\text{ex}} = J_2 \sum_{\langle ij \rangle} (S_z(\mathbf{r}_i)S_z(\mathbf{r}_j) + \frac{1}{2}[S_+(\mathbf{r}_i)S_-(\mathbf{r}_j) + S_-(\mathbf{r}_i)S_+(\mathbf{r}_j)]), \quad (\text{S11})$$

where $S_z(\mathbf{r}_i)$ is the z -component of the spin operator at site \mathbf{r}_i on the lattice, and so on. The goal is to convert the exchange Hamiltonian from spin operators to boson creation/annihilation operators. The spin operator components are found to have the following expansion in terms of boson operators

$$\begin{aligned} S_+(\mathbf{r}) &= f_1 a(\mathbf{r}) + f_2 c^\dagger(\mathbf{r}) + \dots, \\ S_-(\mathbf{r}) &= f_1 a^\dagger(\mathbf{r}) + f_2 c(\mathbf{r}) + \dots, \\ S_z(\mathbf{r}) &= f_3 [b(\mathbf{r}) + b^\dagger(\mathbf{r})] + \dots, \end{aligned} \quad (\text{S12})$$

where only the leading (linear) terms are given. The above expansion is valid in the case of an applied magnetic field along one of the cubic axes, labelled z (the case for a general field orientation will be discussed later). The pre-factors in the expansion, $f_1 = \langle \psi_0 | S_+ | \psi_1 \rangle$, $f_2 = \langle \psi_3 | S_+ | \psi_0 \rangle$ and $f_3 = \langle \psi_0 | S_z | \psi_2 \rangle$, are matrix elements that depend on the wavefunction content of the lowest four states, ψ_{0-3} , which in turn depend on B_4 , λ_0 and the magnetic field strength B . In (S12) we have explicitly included the position dependence of the operators, i.e. $a^\dagger(\mathbf{r})$ creates an a -type boson at site \mathbf{r} and so on.

Substituting (S12) into (S11) gives the spin Hamiltonian as a bilinear form of boson operators. To allow this to be diagonalized to find the normal modes we introduce the Fourier-transformed operators defined by

$$a(\mathbf{r}) = \frac{1}{\sqrt{N}} \sum_{\mathbf{k}} a_{\mathbf{k}} e^{-i\mathbf{k} \cdot \mathbf{r}}, \quad (\text{S13})$$

with similar expressions for $b(\mathbf{r})$ and $c(\mathbf{r})$. Here N is the number of sites in an FCC sublattice. The exchange Hamiltonian expanded up to quadratic order in the bosons reads

$$\mathcal{H}_{\text{ex}} = \sum_{\mathbf{k}} X^\dagger H X + E_0, \quad (\text{S14})$$

where E_0 is a constant, the sum extends all wavevectors \mathbf{k} in the Brillouin zone of the FCC sublattice and the \mathbf{k} dependence of the operator matrix X and of the (Hermitian) Hamiltonian matrix H is implicit. The operator matrix X^\dagger is the row vector

$$X^\dagger = [a_{\mathbf{k}}^\dagger \ c_{\mathbf{k}}^\dagger \ b_{\mathbf{k}}^\dagger \ a_{-\mathbf{k}} \ c_{-\mathbf{k}} \ b_{-\mathbf{k}}], \quad (\text{S15})$$

and X is its adjoint column vector. The Hamiltonian 6×6 matrix H has the block form

$$H = \begin{bmatrix} A_{\mathbf{k}} & B_{\mathbf{k}} \\ B_{\mathbf{k}} & A_{\mathbf{k}} \end{bmatrix}, \quad (\text{S16})$$

where

$$A_{\mathbf{k}} = \frac{1}{2} \begin{bmatrix} \lambda_1 + \frac{f_1^2}{2} J(\mathbf{k}) & 0 & 0 \\ 0 & \lambda_3 + \frac{f_2^2}{2} J(\mathbf{k}) & 0 \\ 0 & 0 & \lambda_2 + f_3^2 J(\mathbf{k}) \end{bmatrix},$$

$$B_{\mathbf{k}} = \frac{J(\mathbf{k})}{2} \begin{bmatrix} 0 & \frac{f_1 f_2}{2} & 0 \\ \frac{f_1 f_2}{2} & 0 & 0 \\ 0 & 0 & f_3^2 \end{bmatrix}, \quad (\text{S17})$$

and $J(\mathbf{k})$ is the Fourier transform of the exchange interactions defined using the convention in [13] as

$$J(\mathbf{k}) = J_2 \sum_{\mathbf{A}} \cos(\mathbf{k} \cdot \mathbf{A}),$$

where the sum extends over all vectors \mathbf{A} linking a Fe^{2+} ion to its 12 nearest neighbors on the same FCC sublattice. $\lambda_{1,2,3}$ denote the energy cost of creating an a -, b -, c -type boson, respectively, at a lattice site in the absence of exchange interactions ($J_2 = 0$), with the three levels being degenerate in zero field. We note that the order of the operators in the row basis vector X^\dagger listed in (S15) was chosen such as to have a block form for the matrix $B_{\mathbf{k}}$ in (S17).

Diagonalizing the Hamiltonian (S16) using standard methods [28] leads to the following dispersion relations for the triplons

$$\hbar\omega_1(\mathbf{k}) = \left[\frac{f_1^2 J(\mathbf{k})}{4} + \frac{\lambda_1}{2} \right] \left[1 - \phi_1 + \sqrt{(1 + \phi_1)^2 - \xi_1^2} \right],$$

$$\hbar\omega_3(\mathbf{k}) = \left[\frac{f_2^2 J(\mathbf{k})}{4} + \frac{\lambda_3}{2} \right] \left[1 - \phi_2 + \sqrt{(1 + \phi_2)^2 - \xi_2^2} \right],$$

$$\hbar\omega_2(\mathbf{k}) = \lambda_2 \sqrt{1 + 2\theta}, \quad (\text{S18})$$

where

$$\phi_1 = \frac{f_2^2 J(\mathbf{k}) + 2\lambda_3}{f_1^2 J(\mathbf{k}) + 2\lambda_1},$$

$$\phi_2 = \frac{f_1^2 J(\mathbf{k}) + 2\lambda_1}{f_2^2 J(\mathbf{k}) + 2\lambda_3},$$

$$\xi_1 = \frac{2f_1 f_2 J(\mathbf{k})}{f_1^2 J(\mathbf{k}) + 2\lambda_1},$$

$$\xi_2 = \frac{2f_1 f_2 J(\mathbf{k})}{f_2^2 J(\mathbf{k}) + 2\lambda_3},$$

$$\theta = \frac{f_3^2 J(\mathbf{k})}{\lambda_2}.$$

In zero field all three modes are degenerate and in the limit $|B_4| \rightarrow \infty$, $|f_1|^2 = |f_2|^2 = 4$ and $|f_3|^2 = 2$, so the triplon dispersion becomes

$$\hbar\omega(\mathbf{k}) = \lambda \sqrt{1 + \frac{4J(\mathbf{k})}{\lambda}}, \quad (\text{S19})$$

in agreement with results deduced using a random-phase approximation [13] and an earlier derivation [1] using a first order expansion in the exchange $\hbar\omega(\mathbf{k}) \simeq \lambda + 2J(\mathbf{k})$.

In order to evaluate the matrix elements for the neutron cross-section from triplons one also needs to know explicitly the transformation matrix \mathbf{Q} to the basis Y of normal operators where the Hamiltonian is diagonal. The transformation matrix \mathbf{Q} needs to satisfy the following three conditions [29]

$$\begin{aligned} \mathbf{Q}g\Lambda\mathbf{Q}^{-1} &= gH, \\ \mathbf{Q}g\mathbf{Q}^\dagger &= g, \\ \mathbf{Q}^\dagger H\mathbf{Q} &= \Lambda, \end{aligned} \quad (\text{S20})$$

where Λ is the diagonal form of the Hamiltonian matrix and \mathbf{g} is the operator commutator matrix

$$\mathbf{g} = [X^\dagger, X].$$

The normal operator basis Y is related to the original operator basis X via

$$X = \mathbf{Q}Y, \quad (\text{S21})$$

where the row vector Y^\dagger contains the normal boson operators

$$Y^\dagger = [a_{\mathbf{k}}'^\dagger \ c_{\mathbf{k}}'^\dagger \ b_{\mathbf{k}}'^\dagger \ a'_{-\mathbf{k}} \ c'_{-\mathbf{k}} \ b'_{-\mathbf{k}}]. \quad (\text{S22})$$

An analytic solution for the matrix \mathbf{Q} that satisfies all three conditions in (S20) is found to be

$$\mathbf{Q} = \begin{bmatrix} \mathbf{Q}_{11} & \mathbf{Q}_{12} \\ \mathbf{Q}_{12} & \mathbf{Q}_{11} \end{bmatrix},$$

where

$$\mathbf{Q}_{11} = \begin{bmatrix} 0 & \frac{-\xi_1}{\sqrt{2A_1(1+\phi_1-A_1)}} & 0 \\ \frac{-\xi_2}{\sqrt{2A_2(1+\phi_2-A_2)}} & 0 & 0 \\ 0 & 0 & \frac{-\theta}{\sqrt{2A_3(1+\theta-A_3)}} \end{bmatrix},$$

$$Q_{12} = \begin{bmatrix} \sqrt{\frac{1+\phi_2}{2A_2} - \frac{1}{2}} & 0 & 0 \\ 0 & \sqrt{\frac{1+\phi_1}{2A_1} - \frac{1}{2}} & 0 \\ 0 & 0 & \sqrt{\frac{1+\theta}{2A_3} - \frac{1}{2}} \end{bmatrix},$$

and

$$\begin{aligned} A_1 &= \sqrt{(1+\phi_1)^2 - \xi_1^2}, \\ A_2 &= \sqrt{(1+\phi_2)^2 - \xi_2^2}, \\ A_3 &= \sqrt{1+2\theta}. \end{aligned}$$

Knowing the transformation matrix Q we can then determine the representation of the \mathbf{L} and \mathbf{S} operators in terms of the basis Y of normal operators as follows. Using (S12) the Fourier-transformed spin operator components $S_\nu(\mathbf{k})$, with $\nu = z, +$ or $-$, can be written in the generic form $S_\nu(\mathbf{k}) = \mathcal{S}_\nu X$, where \mathcal{S}_ν is a row vector of c-numbers, for example $\mathcal{S}_z = [0 \ 0 \ f_3 \ 0 \ 0 \ f_3]$. With respect to the basis of normal operators, the Fourier-transformed spin operator components become $S_\nu(\mathbf{k}) = \mathcal{S}_\nu QY$, with similar expressions for the orbital components $L_\nu(\mathbf{k})$. Subsequently, we can evaluate all matrix elements in (S4) and thus calculate the neutron scattering cross-section in Sec. S6.

S4. WAVEFUNCTIONS IN APPLIED FIELD AND MEAN FIELD APPROXIMATION

In this section we outline the derivation of the singletion states in the presence of an externally-applied magnetic field and exchange interactions, treated within a mean-field approximation following [20]. Focusing on a single site, the relevant Hamiltonian including the singletion terms (S1) and the exchange interactions (S10) is

$$\mathcal{H} = \mathcal{H}_{\text{cf}} + \mathcal{H}_{\text{SO}} + \mu_B \mathbf{B} \cdot (\mathbf{L} + 2\mathbf{S}) + \sum_{\mathbf{A}} J_2 \mathbf{S} \cdot \mathbf{S}_{\mathbf{A}}, \quad (\text{S23})$$

where the sum in the last term extends over all vectors \mathbf{A} linking a Fe^{2+} ion with its 12 NN on the same FCC sublattice. In the mean-field approximation the spin operators $\mathbf{S}_{\mathbf{A}}$ are replaced by their expectation value $\langle \mathbf{S} \rangle$, assumed to be the same for all sites, i.e. we search for self-consistent solutions for the ground state of the single-site mean-field Hamiltonian

$$\mathcal{H}_{\text{mf}} = \mathcal{H}_{\text{cf}} + \mathcal{H}_{\text{SO}} + \mu_B \mathbf{B} \cdot (\mathbf{L} + 2\mathbf{S}) + 12J_2 \mathbf{S} \cdot \langle \mathbf{S} \rangle. \quad (\text{S24})$$

We assume the ansatz

$$\langle \mathbf{S} \rangle = m \hat{\mathbf{B}}, \quad (\text{S25})$$

where the field-induced spin polarization is along the applied field direction, denoted by the unit vector $\hat{\mathbf{B}}$. Using an assumed value for the spin polarization m we diagonalize (S24) to find the ground state wavefunction ψ_0 and

determine the expectation value of the spin polarization for that state

$$m' = \langle \psi_0 | \mathbf{S} \cdot \hat{\mathbf{B}} | \psi_0 \rangle,$$

and search numerically for a self-consistent solution $m' = m$. For this solution we determine the wavefunctions ψ_{0-3} of the four lowest energy eigenstates of the mean-field Hamiltonian (S24). If the field is applied along a cubic axis the spin operator expansions in terms of bosons have the simplified forms in (S12) and the dispersion relations can be obtained analytically as listed in (S18). For a general field direction the spin operator expansions (S12) generalize to contain up to three creation and annihilation terms each, and the 3×3 matrices $A_{\mathbf{k}}$ and $B_{\mathbf{k}}$ in (S17) have in general all elements non-zero. In this case we numerically diagonalize the Hamiltonian matrix in (S16) to deduce the dispersion relations $\hbar\omega_{1-3}(\mathbf{k})$ and the transformation matrix Q to obtain the neutron cross-section.

In the limit of small magnetic fields the behavior is independent of the applied field direction [13], however for the magnitude fields used in the present study there is a significant dependence of the triplon energies on the field orientation with respect to the cubic axes. This anisotropy ultimately originates in the fact that the crystal-field interaction \mathcal{H}_{cf} in (S2) has only cubic, not spherical symmetry. To illustrate this effect we plot in Fig. S2 the dispersion relations along the high-symmetry (100) direction for a magnetic field $B = 8.5$ T applied along the cubic (001) axis (red solid lines) and along the diagonal (111) direction (green dashed lines), respectively. For both field directions the three-fold degeneracy of the spin-orbital triplons is lifted resulting in three non-degenerate modes. The field-dependence of the excitation energies at the zone center (Γ -point) is plotted in Fig. S2b). Here the splitting is approximately linear in field, independent of the field direction and moreover the calculation is in quantitative agreement with no adjustable parameters with the observed splitting of transition lines seen in THz experiments on a powder sample (data points from [15]). At the mode softening wavevector (100) the behavior is very different, non-linear in field, and the energies depend strongly on the applied field direction as illustrated in Fig. S2c). It is the field behavior at those wavevectors that is probed in the low-energy INS signal in Figs. 3a-c) and 4a).

Finally we note that the application of a magnetic field leads to a mixing between the zero-field states shown in Fig. S1, inset) with the consequence that transitions become allowed between the ground state ψ_0 and other higher energy states derived from the E -doublet, in addition to transitions to the first three excited states $\psi_{1,2,3}$. Specifically, this mixing allows transitions between the ground state and high energy states originating from the Γ_3 doublet in Fig. S1 (inset). However, the INS data in applied magnetic field shown in Fig. 3 is restricted to the

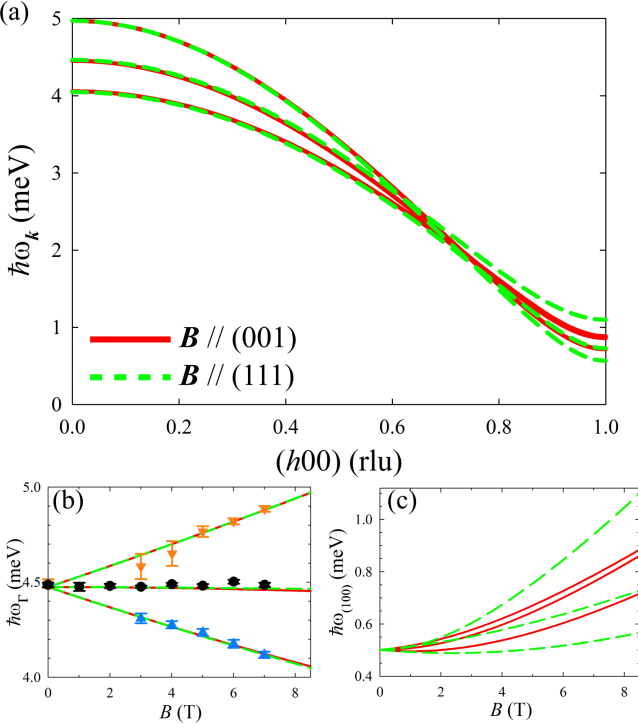


FIG. S2. (Color online) a) Dispersion relations along the (100) direction in reciprocal space for a magnetic field $B = 8.5$ T applied along (001) (solid red lines) and (111) (dashed green lines), respectively. b) Splitting of excitation energies at the zone center is linear in field and independent of direction, in agreement with experimentally-measured THz transition energies on powder samples (data points from [15]). c) In contrast, excitation energies at the softening point (100) show a noticeable dependence on the applied field direction (solid red lines for (001) and dashed green for (111)).

region of low to intermediate energy transfers when only transitions $\psi_0 \rightarrow \psi_{1,2,3}$ contribute, so the approximations used in deriving the dispersion relations and intensities using the three-flavor pseudo-boson method in Sec. S3 are still expected to be applicable.

S5. BACKGROUND SUBTRACTION USING DETAILED BALANCE

In this section we outline the procedure used to estimate the non-magnetic background contribution to subtract from the measured INS data to obtain the pure magnetic signal. The method uses a measured low-temperature data set, where magnetic signal is expected to be present only on the positive energy side, and a data set measured at relatively high temperatures, in the paramagnetic phase, where a weaker, diffuse, magnetic signal is expected to be present on both the positive and negative energy sides. The relative intensities between the positive and negative energy transfer for a given wavevector transfer \mathbf{Q} are related by the principle of detailed

balance for the dynamical structure factor [30]

$$S(-\mathbf{Q}, -\hbar\omega) = e^{-\frac{\hbar\omega}{k_B T}} S(\mathbf{Q}, \hbar\omega). \quad (\text{S26})$$

Formally, this is a consequence of the effect of time-reversal on the dynamical structure factor, whereas physically it expresses the fact that the intensity for a given process which transfers energy $\hbar\omega$ to the neutron is exactly the same as for the reverse process (when the neutron transfers energy $\hbar\omega$ to the system) multiplied by a Boltzmann factor. It is seen that in the limit of $T \rightarrow \infty$ both processes are equally likely and contribute symmetrically to the intensity profile. This principle applies regardless of the potential responsible for the scattering. Eq. (S26) implies the same Boltzmann factor relation between the spherically-averaged structure factors $S(Q, \pm\hbar\omega)$, as relevant for a powder INS experiment.

The application of the principle of detailed balance to estimate the non-magnetic background proceeds as follows; at very low temperatures (2.2 K in the experiments outlined in the main text, Fig. S3(a)), the inelastic scattering is concentrated almost entirely on the $\omega > 0$ side of the dynamical structure factor profile, as there are very few thermally excited levels within the system able to transfer energy to the neutron. As the temperature increases, the scattering intensity spreads to the $\omega < 0$ side as excited states become thermally populated within the system. Assuming that the contribution of magnetic scattering on the $\omega < 0$ side (in practice, below the elastic line) is negligible at base temperature, by subtracting this intensity profile from a high temperature data set (in practice, 50 K was found to be high enough, Fig. S3(b)) one can achieve an estimate for the intensity of magnetic scattering processes that transfer energy to the neutron at 50 K, this subtraction is shown in Fig. S3(c). However, (S26) shows that the intensity on the negative ω side is related to that on the positive ω side at the same Q via the Boltzmann factor. Thereby, through ‘reflecting’ this negative ω intensity profile about the elastic line taking account of the Boltzmann factor in (S26), one arrives at an estimate of the high temperature (50 K) magnetic scattering intensity, shown in Fig. S3(d). The ‘reflection’ of the magnetic signal works well for finite energy transfers away from the elastic line, but is not applicable in the very close vicinity of the elastic line where the signals to be subtracted between the two data sets are very large and so extracting small differences is not sufficiently reliable and/or there could be additional scattering contributions with a distinct temperature dependence, see the clear non-smooth behavior very close to the elastic line in Fig. S3(d). In this case we interpolate the paramagnetic scattering intensity in the region covering the close vicinity of the elastic line by assuming a smooth variation of the diffuse scattering signal between the negative and positive energy sides to obtain the plot in Fig. S3(e). This is illustrated in the

energy scan in Fig. S3(g). The points below -1 meV are from the subtraction 50 K minus 2.2 K data, points above 1.5 meV are obtained via ‘reflection’, and points in-between are interpolated. The solid line in the figure is a fit to the functional form $I(\omega) = f(\hbar\omega/k_B T)G(\omega)$, where $f(x) = x/(1 - e^{-x})$ and $G(\omega)$ is a Gaussian of adjustable width centered at $\omega = 0$. This parametrization was chosen as i) it satisfies the detailed balance principle in (S26), ii) it converges at $T \rightarrow \infty$ to a smooth profile centered at zero energy, as expected for diffuse paramagnetic scattering, and iii) empirically it appears to be a good parametrization of the observed diffuse scattering, as shown by the comparison in Fig. S3(g). The estimated pure magnetic signal at high temperature in Fig. S3(e) is then subtracted from the raw data in panel (a) to obtain the estimated non-magnetic background plotted in panel (f), this in turn is then subtracted from the low-temperature data in panel (b) to obtain the pure magnetic signal plotted in Fig. 2(a).

S6. POWDER-AVERAGED NEUTRON SCATTERING INTENSITY

The inelastic neutron scattering intensity including polarization and magnetic form factors is [30]

$$S(\mathbf{Q}, \hbar\omega) = (\gamma r_0)^2 f(Q)^2 \times \sum_{\alpha, \beta=x, y, z} \left(\delta_{\alpha\beta} - \frac{Q_\alpha Q_\beta}{Q^2} \right) S^{\alpha\beta}(\mathbf{Q}, \hbar\omega), \quad (\text{S27})$$

where $(\gamma r_0)^2 = 290.6$ mbarns/sr is a conversion factor bringing the intensity into absolute units of mbarns/meV/sr/formula unit, and $f(Q)$ is the magnetic form factor for Fe^{2+} ions. Here $Q_{x, y, z}$ are the components of the wavevector transfer \mathbf{Q} along the Cartesian x, y, z axes. $S^{\alpha\beta}(\mathbf{Q}, \hbar\omega)$ contain the dynamical correlations for all possible transitions from an initial state, $|i\rangle$ to a final state $|f\rangle$ given by

$$S^{\alpha\beta}(\mathbf{Q}, \hbar\omega) = \sum_{i, f} p_i \langle i | L_\alpha + 2S_\alpha | f \rangle \langle f | L_\beta + 2S_\beta | i \rangle \times \delta(\hbar\omega + E_f - E_i), \quad (\text{S28})$$

where p_i is the probability of the system initially being in state i , $E_f - E_i$ is the energy transfer for the $i \rightarrow f$ transitions, and the approximation $g_S = 2$ has been used. At base temperature only the ground state is populated, $|i\rangle$ then corresponds to the product of $\psi_0(\mathbf{r})$ states at every site \mathbf{r} in the lattice, and the final states $|f\rangle$ correspond to one-triplon states created by the normal pseudo-boson operators $a_{\mathbf{k}}^{\dagger}, b_{\mathbf{k}}^{\dagger}$ and $c_{\mathbf{k}}^{\dagger}$ in (S22), with the dispersion relations $\hbar\omega_{1,2,3}$ given in (S18).

We note that the dynamical correlations for the spin-orbital singlet state have previously been calculated by treating the exchange J_2 within a random-phase-approximation formalism [20]. Here we have provided

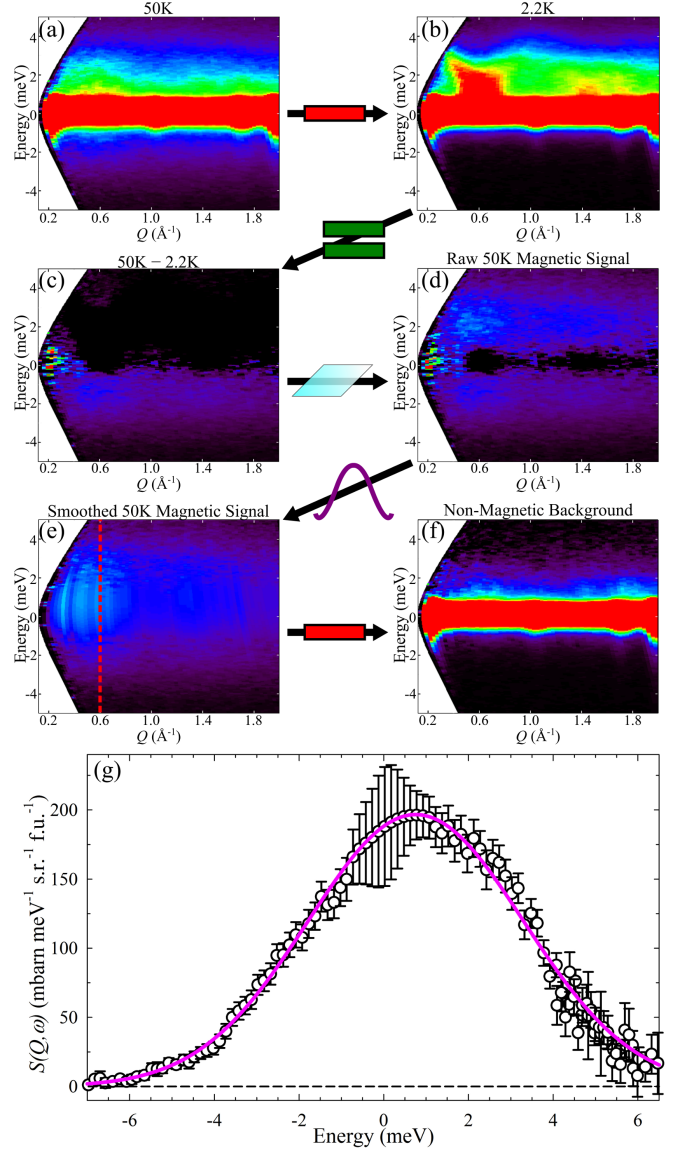


FIG. S3. (Color online) Background subtraction procedure: the base temperature (2.2 K) raw data in (b) is subtracted from the high temperature (50 K) raw data in (a) to obtain (c), which contains pure paramagnetic scattering on the negative energy side. The $\omega < 0$ data in (c) is then ‘reflected’ onto the $\omega > 0$ side using (S26), then interpolated over the elastic line region to obtain the estimated pure paramagnetic scattering in (e), which is then subtracted from the raw data in (a) to obtain the estimated non-magnetic background in (f). (g) Energy scan at $Q = 0.6(1)\text{\AA}^{-1}$ through the estimated pure magnetic signal at 50 K in (e). Solid line is a fit to an empirical functional form that satisfies the detailed balance relation (S26) and is described in the text. Dashed horizontal line emphasizes that plotted intensities are background subtracted.

an alternative approach by deriving directly the dispersion relations in the presence of exchange interactions via pseudo-boson triplon operators and deriving explicitly the neutron scattering structure factor (via the trans-

formation to normal triplon operators) for both zero and applied magnetic field. For zero magnetic field the cross-

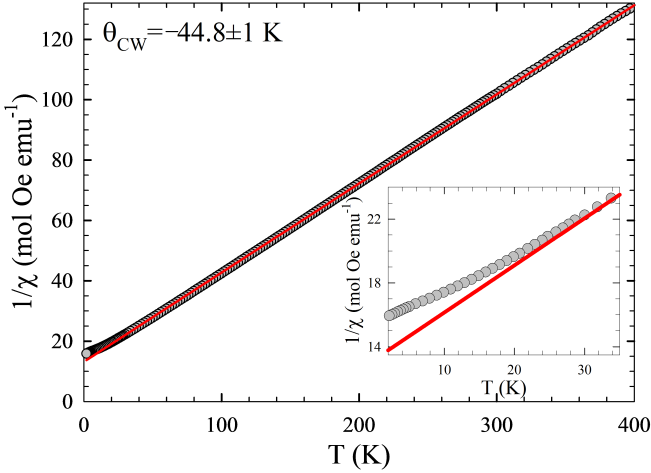


FIG. S4. (Color online) Inverse magnetic susceptibility of FeSc_2S_4 powder as a function of temperature (gray circles) in an applied field of $H = 10^4$ Oe. The thick solid line is a fit to a Curie-Weiss form $\chi = C/(T - \Theta_{\text{CW}})$ giving $\Theta_{\text{CW}} = -44.8 \pm 1$ K. Inset: zoom-in of the low temperature region showing deviation from the linear behavior and the absence of any sharp features indicative of a transition to magnetic order.

section (S27) was numerically averaged over a spherical distribution of orientations of \mathbf{Q} in order to obtain the orientational-averaged intensity as a function of momentum $Q = |\mathbf{Q}|$ and energy transfer, $S(Q, \hbar\omega)$, and this was directly compared with the measured INS powder data in Fig. 2b). In a finite applied magnetic field the dispersion relations (and neutron cross-section) depend on the applied field direction with respect to the cubic axes (as discussed in Sec. S4), so in this case a more elaborate averaging is required to reflect the fact that the powder contains a spherically-uniform distribution of sample grain orientations with respect to the instrument frame, but all grains have the magnetic field applied along a fixed direction with respect to the instrument frame. Since in the experimental geometry used the (vertical) magnetic field was perpendicular to the (horizontal) scattering plane of the detectors ($\mathbf{B} \perp \mathbf{Q}$), the appropriate powder cross-

section is obtained by averaging the single-crystal cross-section (S27) over a uniform distribution of wavevectors \mathbf{Q} on a sphere of radius Q and choosing a uniform random direction of the magnetic field in the plane normal to \mathbf{Q} . This method was used to calculate the INS spectrum in Figs. 3d-f) and 4a) (dashed lines).

S7. SAMPLE PREPARATION

Polycrystalline FeSc_2S_4 was prepared by solid state synthesis from the elements: Fe (99.99%), Sc (99.9%), and S (99.999%). Starting materials were loaded into quartz ampoules under Argon atmosphere, then pumped to 10^{-2} mbar and closed. After first firing at 900°C for 150 h the mixture was reground, pressed into pellets, again closed within an ampoule and fired at the same temperature. To reach full reaction, the sintering procedure was repeated several times (up to 7 cycles). The samples after each cycle were checked by SQUID magnetometry and XRD measurements. To optimize the Fe:Sc:S ratio to the stoichiometric one, additional heat treatments in vacuum and sulfur atmosphere at the last cycles were performed. XRD studies of the final product by conventional powder diffraction (STADI-P, STOE & Cie) did not find any non-reacted impurities or binary sulfides. The Rietveld analysis of the XRD pattern did not reveal essential inversion for cations between A and B sites. The composition of the sample was measured by wave-length-dispersive X-ray electron-probe microanalysis (WDS EPMA, Cameca SX50). The data were averaged over points measured on 15 different single-crystalline grains of about $40 \mu\text{m}$ in diameter. The obtained composition was Fe 1.006(19) Sc 2.000(33) S 3.977(29) and corresponds to perfect stoichiometry (numbers in the brackets give the standard deviations). Results of magnetic susceptibility measurements (SQUID, MPMS-5, Quantum Design) are shown in Fig. S4 and reveal a linear dependence of the inverse susceptibility on temperature over the range ≈ 20 -400 K, in agreement with previous reports [7]. No evidence for magnetic ordering was found down to the lowest temperature probed, 1.8 K.